

Imaging biological tissue with high-throughput single-pixel compressive holography

Wu Daixuan

Sun Yat-Sen University <https://orcid.org/0000-0002-9232-3442>

Luo Jiawei

Sun Yat-sen University

Huang Guoqiang

Sun Yat-sen University

Yuanhua Feng

Jinan University

Feng Xiaohua

University of California

Shen Yuecheng (✉ shenyuecheng@mail.sysu.edu.cn)

Sun Yat-sen University

Zhao-Hui Li

Sun Yat-sen University

Article

Keywords: Single-pixel holography (SPH), holographic images

Posted Date: January 6th, 2021

DOI: <https://doi.org/10.21203/rs.3.rs-129598/v1>

License:  This work is licensed under a Creative Commons Attribution 4.0 International License.

[Read Full License](#)

Version of Record: A version of this preprint was published at Nature Communications on August 5th, 2021. See the published version at <https://doi.org/10.1038/s41467-021-24990-0>.

Imaging biological tissue with high-throughput single-pixel compressive holography

Daixuan Wu,¹ Jiawei Luo,¹ Guoqiang Huang,¹ Yuanhua Feng,² Xiaohua Feng,³ Yuecheng Shen,^{1,*} and Zhaohui Li^{1,4,*}

¹Key Laboratory of Optoelectronic Materials and Technologies, School of Electronics and Information Technology, Sun Yat-sen University, Guangzhou, China, 510275

²Department of Electronic Engineering, College of Information Science and Technology, Jinan University, Guangzhou, China, 510632

³Department of Bioengineering, University of California, Los Angeles, USA, 90095

⁴Southern Marine Science and Engineering Guangdong Laboratory (Zhuhai), Zhuhai, China, 519000

Corresponding authors: shenyuecheng@mail.sysu.edu.cn and lzh88@mail.sysu.edu.cn

Abstract

Single-pixel holography (SPH) is capable of generating holographic images with rich spatial information by employing only a single-pixel detector. Thanks to the relatively low dark-noise production, high sensitivity, large bandwidth, and cheap price of single-pixel detectors in comparison to pixel-array detectors, SPH is becoming an attractive imaging modality at wavelengths where pixel-array detectors are not available or prohibitively expensive. Moreover, SPH is particularly advantageous when imaging through scattering media or in scarce illumination with compressive sensing. In the current practice of SPH, the throughput of the system is mainly limited by the phase-encoded illumination and the ways to realize phase stepping. In this work, we developed a high-throughput single-pixel compressive holography, achieving a space-bandwidth-time product (SBP-T) of 41,667 pixels/s. This result indicates that by using a single-pixel detector, information of holographic images containing up to 65,536 pixels can be collected within only 3 seconds. The high-throughput was realized by enabling phase stepping naturally in time and abandoning the need for phase-encoded illumination. We further show that compressive sensing can be conveniently adapted to significantly reduce the acquisition time. Besides being high throughput, we also show that this holographic system is scalable to provide either a large field of view ($\sim 83 \text{ mm}^2$) or a high resolution ($5.8 \mu\text{m} \times 4.3 \mu\text{m}$). In particular, high-resolution holographic images of a piece of rat tail were presented, exhibiting rich information of mussel, cortical bone, and cancellous bone. Given that microscopic images of biological tissue has rarely been explored in the current practice of SPH, we anticipate the developed high-throughput SPH is promising to nourish the development of multi-spectrum imaging by providing high-quality holographic images for biological tissues.

Introduction

Pixel-array detectors, such as CCD and CMOS cameras, were commonly used in the traditional imaging scheme. However, these detectors are only cost-effective and maintain good performance within certain spectrum range. In contrast to pixel-array detectors, single-pixel detectors have lower dark-noise production, higher sensitivity, faster response time, and a much cheaper price. Moreover, they have been demonstrated with great performance across almost the entire spectrum range. Therefore, single-pixel imaging (SPI), an emerging computational method that employs a single-pixel detector at the receiving end, offers great potential for optical imaging at wavelengths where pixel-array detectors are not available or prohibitively expensive. Instead of acquiring spatial information through parallel detection, SPI relies on using a spatial light modulator (SLM) to display a series of ordered patterns and then computationally reconstruct spatial information from a series of measurements. Without compressive sensing, the number of effective pixels in the reconstructed image equals the number of ordered patterns being displayed. Since the first demonstration called flying-spot camera in 1884 by Nipkow *et al.* [1, 2], SPI has been later demonstrated with advantages when imaging through scattering media [3-5] or in scarce illumination with compressive sensing [6, 7]. By employing various coding mechanisms including Hadamard bases [5, 8-20], Fourier bases [9, 21-23], and random patterns [24], SPI has also been extended and demonstrated with great success in full-color imaging [10], multispectral imaging [11], and time-resolved imaging [12].

From the perspective of optical imaging, the successful modeling of complex-valued biological samples with both amplitude and phase information is of great significance in biophotonics. For example, many thin biological tissues exhibit low scattering and absorption when interacting with light, leading to low contrast when being directly imaged with a conventional microscope. Even for

1 relatively thick tissues whose amplitude images can provide enough contrast, their corresponding phase images always serve as a good
 2 supplement. Since the fast oscillation of the diffracted light prohibits direct measurement of phase information using modern optical
 3 detectors, there is a strong desire to develop an efficacious imaging modality that can provide complex-valued images to study the
 4 microscopic structures of a myriad of biological tissues [25-29]. This capability can also benefit a variety of applications in adaptive
 5 optics [30, 31], surface contour [32, 33], wavefront sensing [34, 35], optical metrology [36-38], and ultrafast optics [39-41].

6 To beat down the fast oscillation of the diffracted light to the regime that modern detectors can reach, holographic approaches that
 7 employ additional reference beams become one of the most effective and intuitive ways to retrieve field information [42-44]. Thus, when
 8 combined with this approach, SPI can be further generalized to extract complex-valued information from the sample, naming single-
 9 pixel holography (SPH). Back in 2013, Clemente *et al.* developed a framework for using a liquid-crystal-based SLM and a bucket single
 10 pixel to image phase objects [13]. Later, digital micromirror devices (DMDs) were employed as the dominant devices to increase the
 11 illumination speed. With DMDs, fast fluorescence imaging and phase imaging were simultaneously realized in a compact SPH system
 12 [17]. People also explored several modifications to boost the performance of SPH, including choosing appropriate orders of various
 13 illumination patterns for compressive sensing [9, 45] and developing common-path interference for robustness [15-18]. Table 1
 14 summarizes the performance of SPI [5, 9-12, 21] and SPH [13-20, 22, 23] reported in the literature. As systems of SPI were developed
 15 in the early years, liquid-crystal-based SLMs were usually employed. Although being slow in the refresh rate, these SLMs can
 16 simultaneously modulate lots of pixels independently, allowing $256 \times 256 = 65,536$ pixels in the reconstructed images to be frequently
 17 obtained [9]. Moreover, these systems were generally designed to image macroscopic objects with a relatively large field of view (FOV).
 18 As a comparison, systems of SPH systems prefer using DMDs with fast refresh rates [17-20, 22, 23]. However, DMDs support only
 19 binary-amplitude modulation so that phase stepping inherent in holography has to be realized at the cost of available pixels through Lee
 20 hologram [46] or superpixel method [47]. As a result, it is conspicuous that the number of pixels in the reconstructed images with SPH
 21 (the largest one is $128 \times 128 = 16,384$ [13, 17, 18]) is normally smaller than that with SPI. For a convenient and straightforward
 22 comparison of SPH systems, some key parameters were highlighted in blue with asterisks. For example, the best lateral resolution was
 23 reported by Shin *et al.* as $0.4 \mu\text{m} \times 0.4 \mu\text{m}$ [18], while the largest FOV was reported by Hu *et al.* as $11.7 \text{ mm} \times 11.7 \text{ mm}$ [22]. Since there
 24 always exists a trade-off among imaging speed, FOV, and lateral resolution, it is inappropriate to compare the performance according to
 25 only one performance index. A figure-of-merit parameter, defined as the space-bandwidth-*time* product (SBP-*T*) [48, 49], can be used
 26 for a fair comparison of SPI/SPH, which represents the throughput of the system. Mathematically, SBP-*T* is computed as the number of
 27 pixels in the reconstructed image divided by the total acquisition time consumed, accounting for the information collected per unit time.
 28 For SPH, an additional factor of 2 is multiplied in the consideration for both the amplitude and the phase. By going through Tab. 1, the
 29 largest SBP-*T* that has been achieved with SPH before this work was 14,667 [23].

30
 31 **Table. 1 List of the parameters in both single-pixel imaging and single-pixel holography.**

	Ref.	Illumination device		Modulation pattern		Total acquisition time (s)	Resolution (μm)	FOV (mm)	SBP- <i>T</i> (pixels/s)	Biological sample?
		Pixel size (μm)	Refresh time (ms)	Number of pixels	Measurements					
Single-pixel imaging	[10]	NA	1.54	$256 \times 128 = 32768$	32768	50.46	≈ 780	200×100	650	No
	[21]	NA	150	$245 \times 245 = 60025$	120052	18007.8	≈ 653	160	3.3	No
	[11]	13.68	20	$64 \times 64 = 4096$	4096	81.9	≈ 703	45	50	No
	[9] (large FOV)	13.68	0.5	$256 \times 256 = 65536$	131072	65.6	≈ 781	≈ 200	1000	No
	[9] (high resolution)	5.4	200	$256 \times 256 = 65536$	131072	26216	5.47	1.4	2.5	No
	[12]	13.68	1000	$64 \times 64 = 4096$	4096	4096	NA	NA	1	No
	[5]	NA	0.05	$32 \times 32 = 1024$	1024	0.0512	NA	NA	20000	No

Single-pixel holography	[13]	19	≈ 13.89	$128 \times 128 = 16384^*$	16384	≈ 227.6	19	2.4	144	No
	[14]	20	≈ 16.67	$64 \times 64 = 4096$	4096	≈ 68.3	160	10.2	120	No
	[19]	13.68	≈ 0.0455	$64 \times 64 = 4096$	16384	≈ 0.7447	≈ 52.5	3.4	11000	No
	[20]	13.68	0.5	$64 \times 64 = 4096$	16384	8.192	≈ 52.5	3.4	1000	Yes*
	[17] (large FOV)	13.68	0.05	$128 \times 128 = 16384^*$	49152	2.5	≈ 82	≈ 10.5	13333.4	No
	[17] (high resolution)	13.68	0.05	$128 \times 128 = 16384^*$	49152	2.5	≈ 12.5	≈ 1.6	13333.4	No
	[18]	13.68	0.1	$128 \times 128 = 16384^*$	49152	4.9	$\approx 0.4^*$	≈ 0.052	6666.8	No
	[15]	20	100	$16 \times 16 = 256$	1024	102.4	476.3	7.62	5	No
	[22]	10.8	0.0562	$81 \times 81 = 6561$	26244	1.5	144	11.7^*	8896.8	No
	[16]	13.68	0.0455	$64 \times 64 = 4096$	16384	≈ 0.7447	109.5	7	11000	No
	[23]	13.68	0.0455	$103 \times 103 = 10609$	31827	≈ 1.448	68.4	7	14666.6	No
	This work (large FOV)	13.68	0.048	$256 \times 256 = 65536^*$	65536	3.14	58.0×43.1	$14.9 \times 11.1^*$	41666.6^*	No
This work (high resolution)	13.68	0.048	$256 \times 256 = 65536^*$	65536	3.14	5.8×4.3	1.5×1.1	41666.6^*	Yes*	

The key parameters that represent the most advanced indexes in SPH before and after this work were are highlighted with asterisks in blue and red, respectively. NA: not applicable

Two major factors limit the throughput of SPH in current practice: (1) the phase stepping inherent in holography required a few patterns being displayed for each order, thus inevitably slowing down the imaging process; (2) both the Lee hologram and the superpixel method were realized at the cost of independent pixels, therefore reducing the number of effective pixels in the reconstructed image. In this work, we overturn this practice by developing high-throughput SPH. Instead of actively performing phase shifting, a beat frequency is introduced between the signal beam and the reference beam, thereby realizing phase stepping naturally in time by exploiting the framework of heterodyne holography. Moreover, instead of generating phase patterns with DMDs by scarifying pixels, we show both theoretically and experimentally that non-orthogonal binary-amplitude Hadamard patterns can be used for holographic reconstruction as well. Thus, by directly projecting the desired amplitude patterns to the sample, the developed high-throughput SPH can achieve an SBP- T of 41,667 pixels/s, which is about three times larger than the largest one reported in the literature [23]. It is worth noting that this value was achieved using a single-pixel detector. Moreover, the number of pixels in the reconstructed image can be up to $256 \times 256 = 65,536$, which is about four times larger than the largest one reported with SPH before. The developed holographic system can be adapted for different application scenarios by functioning under different operational modes. For example, we can operate under large-FOV mode ($14.9 \text{ mm} \times 11.1 \text{ mm}$) to monitor the environment [9, 10, 21] or switch to high-resolution mode ($5.8 \mu\text{m} \times 4.3 \mu\text{m}$) to scrutinize microstructures [18, 20]. In the microscopic world, one of the most imperative tasks is to image biological tissue. Unfortunately, however, to date, applying SPI/SPH to imaging microscopic structures in biological tissue has been barely reported, mainly due to the limited performance of the imaging system and the relatively low scattering contrast of biological samples. Until very recently, González et al. employed SPH to image the wing of an insect with a lateral resolution of $52.5 \mu\text{m}$ [20]. This regrettable situation considerably hinders SPI/SPH from being widely adopted in biophotonics. Here, we bridge the gap by imaging a piece of rat tail and revealing its rich structures with SPH. The FOV and the lateral resolution of the corresponding figure are $1.5 \text{ mm} \times 1.1 \text{ mm}$ and $5.8 \mu\text{m} \times 4.3 \mu\text{m}$, respectively. This work constitutes an important step towards future high-throughput image modalities using a single-pixel and shows great promise of applying SPI/SPH to image microscopic structures of biological tissue.

Principle of high-throughput single-pixel holography

1 We first describe the operating principle of the high-throughput SPH. Mathematically, the sample to be imaged is described by a
 2 complex function $O(\vec{r}) = A(\vec{r})e^{i\phi(\vec{r})}$, where $A(\vec{r})$ represents the spatially-varying transmissivity and $\phi(\vec{r})$ denotes the accumulated
 3 phase during light propagation. SPI relies on the fact that $O(\vec{r})$ can be decomposed using a set of orthogonal Hadamard bases $H_n(\vec{r})$
 4 that only contains the values of “+1” and “-1”

$$5 \quad O(\vec{r}) = A(\vec{r})e^{i\phi(\vec{r})} = \frac{1}{\sqrt{N}} \sum_n a_n e^{i\varphi_n} H_n(\vec{r}) \quad (1)$$

6 where $1/\sqrt{N}$ is the normalization constant. By exploiting the orthogonality of Hadamard bases, the complex-valued coefficient
 7 $a_n e^{i\varphi_n}$ can be obtained by taking the spatial summation of all the transmitted field over the sample surface S when $H_n(\vec{r})$ is projected:

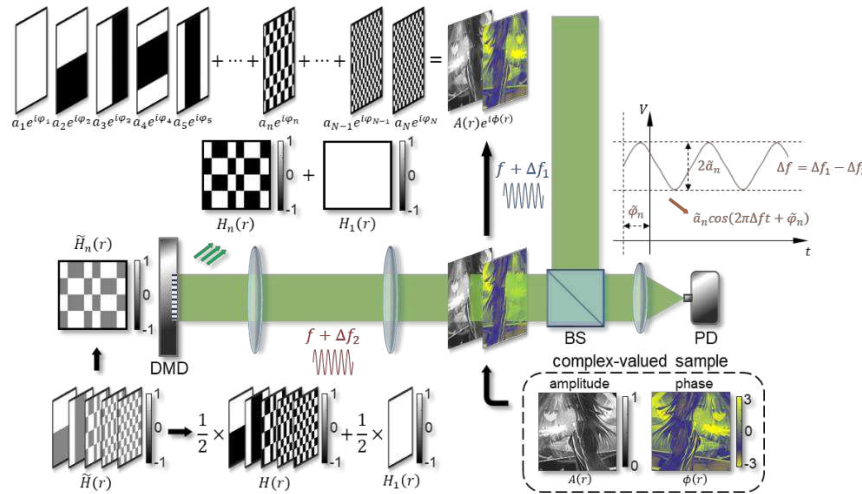
$$8 \quad a_n e^{i\varphi_n} = \frac{1}{\sqrt{N}} \int_S O(\vec{r}) H_n(\vec{r}) dS \quad (2)$$

9 Equation (2) indicates that the successful operation of SPH requires sequentially projecting Hadamard-encoded illumination and
 10 measuring the corresponding transmitted field on the single pixel. However, DMDs with fast refresh rates can only generate Hadamard-
 11 like patterns $\tilde{H}_n(\vec{r})$ with the values of “+1” and “0”. Since a series of $\tilde{H}_n(\vec{r})$ do not form orthogonal bases, the mathematical
 12 relationship in Eqs. (1) and (2) does not hold. To modulate phase using DMDs, previous works employed either Lee hologram or
 13 superpixel method at the cost of available pixels [17-20], thereby limiting the throughput. Fortunately, we show in the following that
 14 generating phase patterns is not necessary for SPH. As shown in Fig. 1, $H_n(\vec{r})$ and $\tilde{H}_n(\vec{r})$ are closely related through $H_n(\vec{r}) =$
 15 $2\tilde{H}_n(\vec{r}) - \tilde{H}_1(\vec{r})$ or $\tilde{H}_n(\vec{r}) = (H_n(\vec{r}) - H_1(\vec{r}))/2$. Here, $\tilde{H}_1(\vec{r})$ is the first order of Hadamard-like patterns, which refers to a term of
 16 direct current. Thus, Eq. (2) can be rewritten as

$$17 \quad a_n e^{i\varphi_n} = \frac{2}{\sqrt{N}} \int_S O(\vec{r}) \tilde{H}_n(\vec{r}) dS - \frac{1}{\sqrt{N}} \int_S O(\vec{r}) \tilde{H}_1(\vec{r}) dS \quad (3)$$

$$= 2\tilde{a}_n e^{i\tilde{\varphi}_n} - \tilde{a}_1 e^{i\tilde{\varphi}_1}$$

18 Here, $\tilde{a}_n e^{i\tilde{\varphi}_n}$ is the spatial summation of all the transmitted field over the sample S when $\tilde{H}_n(\vec{r})$ is projected. This equation
 19 indicates that the complex-valued coefficient $a_n e^{i\varphi_n}$ can be determined by sequentially displaying Hadamard-like patterns $\tilde{H}_n(\vec{r})$ as
 20 well, without the need to illuminate Hadamard bases $H_n(\vec{r})$. To measure the transmitted complex field, both the common-path
 21 interferometry and the Mach-Zander interferometry were employed in previous works [13-20, 22, 23]. In these systems, phase stepping
 22 was realized by either directly inserting a phase plate [13-15] or exploiting combined superpixels [16-20, 22, 23]. Given the current
 23 bottleneck of the imaging speed is limited by the refresh rate of the illumination rather than the bandwidth of the detector, we propose
 24 to implement heterodyne holography to realize phase stepping naturally in time. As shown in Fig. 1, the heterodyne signal oscillates as
 25 $\tilde{a}_n \cos(2\pi\Delta f t + \tilde{\varphi}_n)$, where a beat frequency Δf is introduced between the signal beam and the reference beam. By performing a series
 26 of measurement to the beating signal, both the amplitude a_n and the initial phase φ_n can be uniquely determined (detailed in the
 27 Supplement). The major advantage of implementing this scheme for holography is that only one Hadamard pattern is displayed for each
 28 order as phase stepping is realized naturally in time, thus significantly saving acquisition time and pixel numbers.



29 **Fig. 1 Principle diagram of the high-throughput single-pixel compressive holography.** A complex-valued object $O(\vec{r}) = A(\vec{r})e^{i\phi(\vec{r})}$ can be expressed as
 30 the superposition of a complete set of orthogonal Hadamard basis $H_n(\vec{r})$ with corresponding coefficients. To retrieve these coefficients, one can illuminate the
 31 object with a series of Hadamard-like patterns $\tilde{H}_n(\vec{r})$ (with components “0” and “1”) generated by the DMD. To implement heterodyne holography, a beat
 32

frequency Δf is introduced between the signal beam and the reference beam, enabling a time-varying signal that can be measured by the photodiode. The simple linear transformation between $\tilde{H}_n(\vec{r})$ and $H_n(\vec{r})$ allows the reconstruction of holographic images with pure amplitude patterns. DMD: digital micromirror device; BS: beam splitter; PD: photodiode.

Experimental setup

The experimental setup is schematically shown in Fig. 2. As a demonstration of principle, a long-coherence solid-state semiconductor laser (MSL-FN-532-100mW) that operates at 532 nm was used as the light source. After passing through a polarizing beam splitter (PBS), the light source was divided into a signal beam and a reference beam. A half-wave plate was placed in front of the PBS to adjust the intensity ratio of the two beams. To maximize the visibility of the fringes and achieve a good signal-to-noise ratio during experiments, the desired intensity ratio that reaches the single-pixel detector is 50:50. Heterodyne holography was realized by using two acousto-optic modulators (AOMs), which were controlled by a function generator. In this setup, AOM1 in the reference beam shifted optical frequency by 50 MHz + 31,250 Hz, while AOM2 in the signal beam shifted optical frequency by 50 MHz - 31,250 Hz. Thus, the beat frequency of these two beams is 62,500 Hz, indicating a temporal period of 16 μ s. After frequency modulation, both beams were expanded by a pair of lenses with 7.5-mm and 250-mm focal lengths. The signal beam was then diffracted by a DMD (V7001 DLP7000&DLPC410) to achieve binary-amplitude modulation. This DMD has 768 \times 1024 pixels with 13.68- μ m pixel size and 22-kHz refresh rate. Since the DMD diffracts light like a two-dimensional shining grating, the optimum incident and diffracted angles are calculated to be 17.92 $^\circ$ and 41.92 $^\circ$ (detailed in the supplement). A 4f system that consists of two lenses (scalable due to different operational modes) then imaged the surface of the DMD onto the sample. After interacting with the sample, the signal beam was combined with the reference beam through a beam splitter. It is worth mentioning that since the DMD slightly altered the polarization after modulation, a quarter-wave plate (not shown in the figure) was inserted in the reference beam to maximize the interference visibility. Using a lens with 150-mm focal length, the combined light was then collected by a photodiode, which was then digitized by a data acquisition card (USB-6251, National Instrument) with a sampling rate of 1.25 Ms/s (not shown in the figure). Considering the 48- μ s refresh time of the DMD and the 62,500-Hz beating frequency, 3 beating cycles last for each Hadamard pattern and 20 data points were acquired within one cycle.

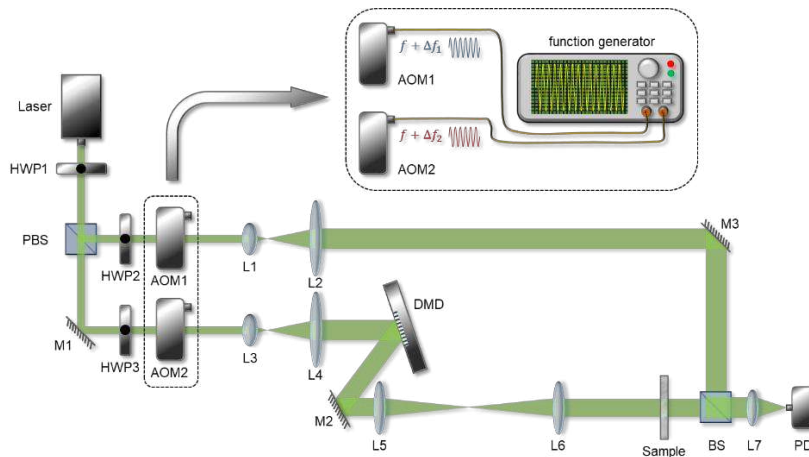


Fig. 2 Experiment setup of the high-throughput single-pixel compressive holography system. A series of Hadamard-like patterns were generated and projected to the sample. HWP1-3: half-wave plate; M1-3: mirror; PBS: polarization beam splitter; AOM1-2: acousto-optic modulators that cause a frequency shift to the light passing through; L1-7, lenses ($f_1 = f_3 = 7.5$ mm, $f_2 = f_4 = 250$ mm, $f_7 = 150$ mm, f_5 and f_6 is scalable to be adapted for various demands); DMD: digital micromirror device that provides amplitude modulation with “0” and “1”; BS: beam splitter; PD: photodiode. The upper inset shows the detailed procedure of how a double-channel function generation generates a beating frequency to drive the AOMs (an electronic power amplifier is omitted here).

For different imaging applications, the FOV and the lateral resolution can be adjusted by either choosing the appropriate lens pair in the 4f system or selecting different binning strategies of the pixels. As a concrete example, the two lenses in the 4f system shown in Fig. 2 have the same focal length of 125 mm, indicating that Hadamard patterns displayed by the DMD were 1:1 imaged onto the surface of the sample. In this condition, if we make full use of the active area by adopting the strategy of binning 3 \times 3 pixels into 256 \times 256 superpixels, this system is expected to have a large FOV of 14.9 mm \times 11.1 mm with a lateral resolution of 58.0 μ m \times 43.1 μ m (large-

FOV mode). The difference in the FOV and lateral resolution along different directions is caused by the 45° -tilted arrangement of the DMD, which is described in detail in the supplement. The operation of the imaging system can also be altered into a high-resolution mode for microscopy by employing two lenses with 300-mm and 30-mm focal lengths in the $4f$ system. Since Hadamard patterns were shrunk by 10 times, the lateral resolution becomes $5.8 \mu\text{m} \times 4.3 \mu\text{m}$ at the cost of the FOV. Nonetheless, since we fixed the highest order of Hadamard patterns to be 256×256 during experiments (limited by the available RAM of the DMD), the throughput of the holographic system remains the same for different modes.

Result

To examine the performance of the holographic system, a standard positive 1951-USAF resolution test target (Thorlabs R3L3S1P) was used as the sample. Firstly, the system was operated under the large-FOV mode. Both strategies of using 768×768 pixels with 3×3 binning and 512×512 pixels with 2×2 binning are applied to verify the performance and scalability of the system. For the first binning strategy, the FOV and the lateral resolution are reported above. Thus, element 4 of group 3 ($44.25\text{-}\mu\text{m}$ width) in the resolution target is the finest structure that can be identified. During experiments, 65,536 Hadamard-like patterns were sequentially displayed and the total imaging process only took 3 seconds. Figures 3(a) and (b) show the reconstructed complex-valued images for groups 2 to 4 of the resolution target, including both the amplitude and phase. As shown in the upper inset of Fig. 3(a), the amplitude image with a smaller FOV to magnify element 4 of group 3 is captured by a conventional microscope. For visualization purposes, the corresponding one-dimensional (1D) profile denoted by the red bracket within the resolution target is shown in the inset below, exhibiting three well-separated narrow dips (vertical lines), one wide dip (horizontal line), and one narrow dip (bottom area of “4”). This result demonstrates that the resolution achieved by using our system meets theoretical expectations. Although the contrast of the phase imaging is not as good as its amplitude companion possibly due to insufficient SNR, similar structures belong to element 4 of group 3 can be observed as well. Corresponding 1D profile of phase image at the same position is also provided in the inset. Regarding the second binning strategy, the FOV and lateral resolution shrink to $9.9 \text{ mm} \times 7.4 \text{ mm}$ and $38.7 \mu\text{m} \times 28.8 \mu\text{m}$, and the corresponding imaging results were provided in the supplement.

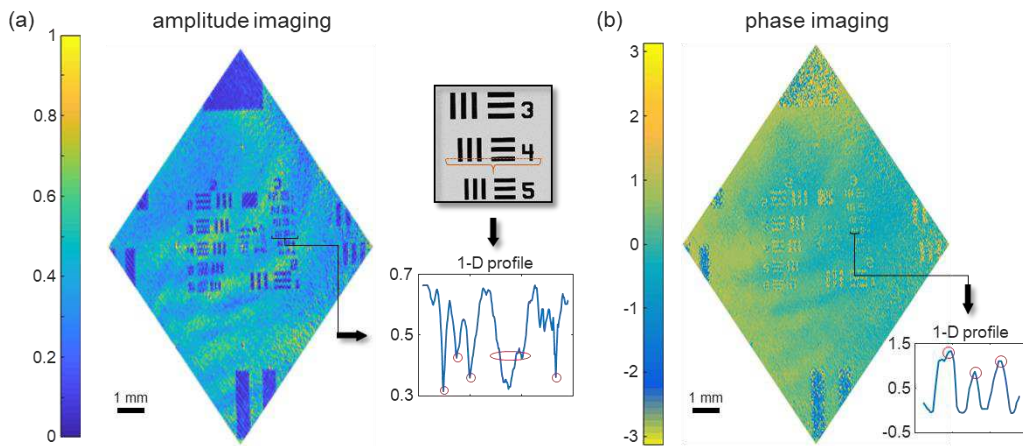
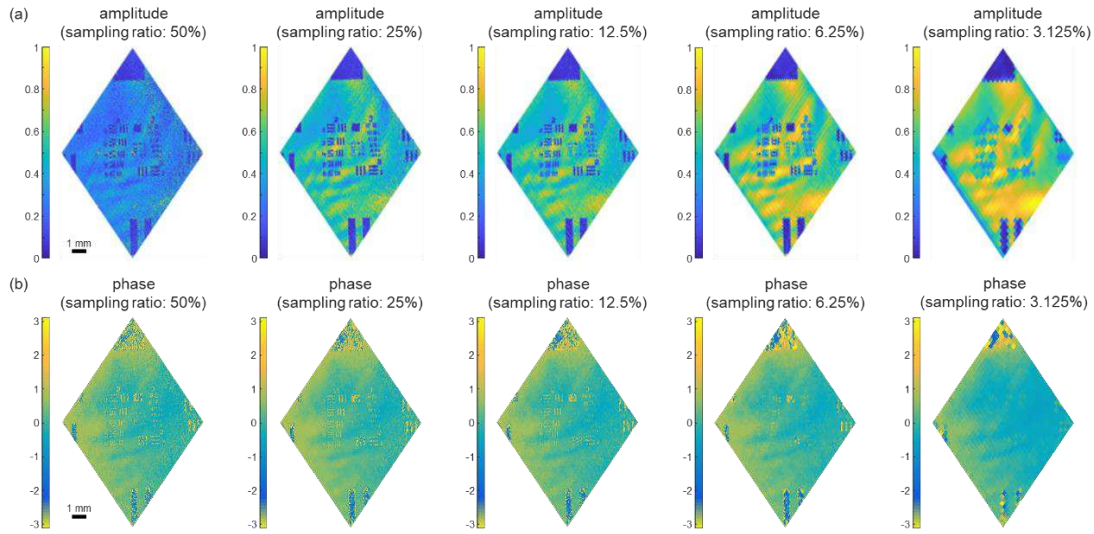


Fig. 3 Performance of the high-throughput SPH in large FOV mode. A standard positive 1951-USAF resolution test target (Thorlabs R3L3S1P) is used as a testing sample. 3×3 pixels binning strategy was adopted for 768×768 pixels, leading to 256×256 superpixels. (a) Reconstructed amplitude image of the resolution target. The upper inset: the image captured by conventional microscopy; the lower inset: the corresponding one-dimensional (1D) profile of element 4 of group 3. (b) Reconstructed phase image of the resolution test target. The corresponding 1D profile is shown in the inset

To further facilitate the imaging process, compressive sensing can be used. To be consistent with the general significance of natural scenes, several orderings of Hadamard bases have been demonstrated previously. Depending on the uniqueness of each sample, these orderings exhibit slightly different performance [45, 50]. In this work, we chose to use a square sampling path (detailed in the supplement). Figure 4 shows the reconstructed amplitude and phase imaging using a different sampling ratio (SR), defined as the ratio between the number of measurements used for reconstruction and the number of pixels in the reconstructed image. For the series of amplitude images in Figs. 4(a), most of the structures in group 3 are still identifiable, even when the SR was decreased to 6.25%. Moreover, since a smaller SR is usually accompanied by a higher contrast-to-noise ratio (CNR), the amplitude image reconstructed with

1 12.5% SR look even better than those reconstructed with 50%. However, when the sampling ratio was further reduced to 3.125%,
 2 artifacts emerge so that no clear lines can be identified. Nonetheless, this observation confirms that by properly selecting the SR,
 3 compressive sensing can greatly shorten the acquisition time without sacrificing too much imaging quality. The series of phase images
 4 reconstructed with various SRs are shown in Figs. 4(b). As long as the $SR \geq 12.5\%$, the quality of the phase images is still acceptable.



5
 6 **Fig. 4 Reconstruction of holographic images for the resolution target with compressive sensing.** The amplitude and wrapped phase images are
 7 reconstructed with different sampling ratios of 50%, 25%, 12.5%, 6.25%, 3.125%.

8
 9 Having demonstrated operating at large-FOV mode, we then switched to the high-resolution mode by changing the lens pair in the
 10 $4f$ system. The strategy of using 768×768 pixels with 3×3 binning is also applied to guarantee light delivery. It is estimated that the
 11 FOV and the lateral resolution are $1.5 \text{ mm} \times 1.1 \text{ mm}$ and $5.8 \mu\text{m} \times 4.3 \mu\text{m}$, respectively, which make this holographic system well suited
 12 for imaging biological samples. We then examined its performance by imaging the resolution target, as shown in Fig. 5(a). For
 13 visualization purposes, the 1D profile of element 6 of group 6 ($4.386\text{-}\mu\text{m}$ width, denoted with a black bracket) is plotted in the lower
 14 inset. One wide dip and three separated narrow dips can be identified, which is consistent with the same structure measured by a
 15 conventional microscope (the upper inset). Then, we proceed to image biological tissue. Figure 5(b) shows the image of a slice of stained
 16 tissue from a rat tail, captured using a bright-field microscope. In this image, several different types of tissue such as mussel, cortical
 17 bone, and cancellous bone are marked. Figures 5(c), (d), and (e) show a series of reconstructed holographic images for different parts
 18 of the stained tissue, indicated by three labeled diamond-shaped boxes in Fig. 5(b). For each part, 65,536 Hadamard patterns were
 19 sequentially displayed and the data acquisition took about 3 seconds. It is conspicuous that all three amplitude images show lots of
 20 intricate details and are in good agreement with the one in Fig. 5(b), manifesting great distinctions among different types of tissue. For
 21 stained tissue, the reconstructed phase images are analogous to their amplitude companions. Nonetheless, these phase images still
 22 supplement with additional information, with some examples encircled in red. These images demonstrate that the developed high-
 23 throughput SPH is capable of revealing delicate microscopic structures of biological tissue.

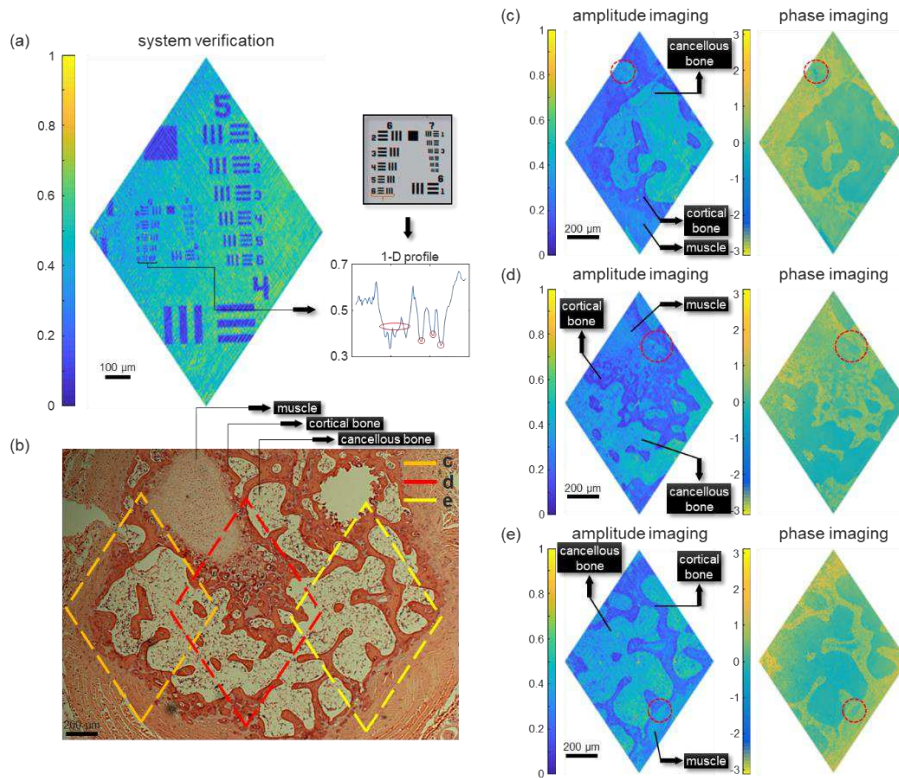


Fig. 5 Performance of the high-throughput SPH in high-resolution mode. (a) Reconstructed amplitude image of a resolution target. The upper inset: the image of the resolution target (containing groups 6 and 7) captured by a conventional microscope; the lower inset: the corresponding one-dimensional (1D) profile of element 6 of group 6. (b) The image of a slice of stained tissue from rat tail, captured using a conventional microscope. Three diamond-shaped boxes represent the area being measured by the holographic system. (c)-(e) The reconstructed amplitude and phase images for different parts of the stained tissue.

We also applied compressive sensing for imaging biological tissue. As a typical example, we targeted the area that corresponds to that in Fig. 5(e). The reconstructed amplitude and phase images using various SRs are illustrated in Figs. 6(a) and (b), respectively. In general, for both amplitude and phase images, the smaller the SR, the less detailed structures can be visualized. These images demonstrate the effectiveness of compressive sensing with small SRs when dealing with biological samples that contain rich detailed information.

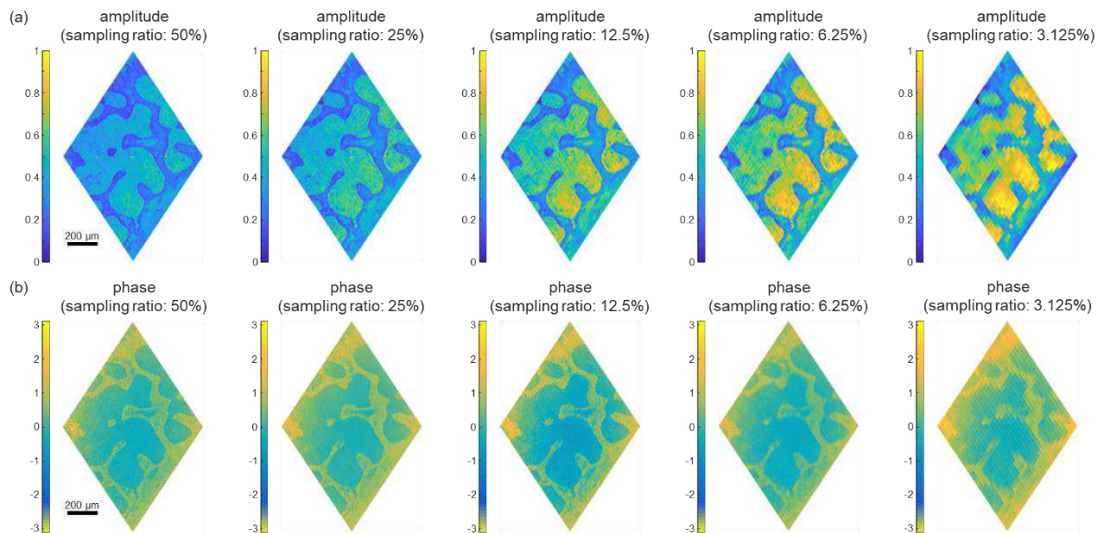


Fig. 6 Reconstruction of holographic images for the piece of rat tail with compressive sensing. The amplitude and wrapped phase images are reconstructed with different sampling ratios of 50%, 25%, 12.5%, 6.25%, 3.125%.

Discussion

In this work, the highest Hadamard patterns being displayed is 65,536, restricting the number of pixels in the reconstructed image

1 to be 256×256 . Such a crucial factor is limited by the finite on-board memory of the DMD (64 Gbits), leading to insufficient usage of
2 its 1024×768 independent micromirrors. Therefore, expanding the on-board memory of the DMD is the key to further increase the
3 number of pixels in the reconstructed image. Moreover, given finite laser power and inevitable energy loss of the holographic system,
4 we noticed that light delivered to the sample is not strong and the measured signal contrast is just around the edge when retrieving
5 coefficients for high orders. Taking the high-resolution mode as an example, the light intensity being projected onto the biological tissue
6 is only 6 mW/cm^2 , which is about 33 times below the ANSI safety limit (200 mW/cm^2). These values also explain why a 3×3 binning
7 was adopted for 768×768 pixels to boost light delivery to biological tissue during the experiments. Therefore, to adapt high-order
8 Hadamard patterns, future works will focus on increasing the laser power and minimizing energy loss of the holographic system. As a
9 final remark, we note that although only two operational modes, i.e., large-FOV and high-resolution modes, were demonstrated, the
10 imaging parameters of this single-pixel holographic system are scalable to other values, either by choosing different pair of lenses in the
11 $4f$ system (physically) or using different pixel binning strategy of the DMD (digitally).

13 Conclusion

14 In this work, we developed high-throughput SPH and imaged biological tissue with high resolution. To realize phase stepping, we
15 creatively introduced heterodyne holography into SPH by using two acousto-optic devices with slightly different modulation frequencies,
16 which dramatically increases the amount of information collected per second. For many imaging indicators, such as FOV, lateral
17 resolution, number of pixels, and SBP- T , the developed holographic system here is among the top of the existing systems of SPH (see
18 Tab. 1). Moreover, the throughput of our system reaches an SBP- T of 41,667 pixels/s, thus being at least three times larger than the
19 largest one reported in literature [23]. Experimentally, we demonstrated the performance of this holographic system under large-FOV
20 mode and high-resolution mode, by successfully imaging a standard resolution target and a piece of biological tissue (rat tail). The
21 imaging results of rat tail show that SPH serves as an effective imaging tool for studying biological tissue that typically requires high
22 resolution and good SNR. We envision that the developed high-throughput SPH is promising to promote multi-spectrum imaging by
23 providing high-resolution complex-valued images for a variety of biological tissues within a broad spectrum range.

26 Funding

27 This work was supported by National Key Research and Development Program of China (2018YFB1802300) and National Natural
28 Science Foundation of China (12004446, 61525502)

30 Reference

- 31 1. P. Nipkow, "Elektrisches teleskop [Electric telescope]," K. Patentamt, ed. (1884), p. 105.
- 32 2. P. Sen, B. Chen, G. Garg, S. R. Marschner, M. Horowitz, M. Levoy, and H. P. Lensch, "Dual photography," in *ACM*
33 *SIGGRAPH 2005 Papers*(2005), pp. 745-755.
- 34 3. E. Tajahuerce, V. Duran, P. Clemente, E. Irlles, F. Soldevila, P. Andres, and J. Lancis, "Image transmission through
35 dynamic scattering media by single-pixel photodetection," *Optics Express* **22**, 16945-16955 (2014).
- 36 4. V. Durán, F. Soldevila, E. Irlles, P. Clemente, E. Tajahuerce, P. Andrés, and J. Lancis, "Compressive imaging in
37 scattering media," *Optics Express* **23**, 14424-14433 (2015).
- 38 5. J. Sudyka, M. Hamkato, and M. Wojtkowski, "Application of single-pixel camera for imaging in turbid media," in
39 *Optical Manipulation and Its Applications*(Optical Society of America2019), p. JT4A. 26.
- 40 6. M. F. Duarte, M. A. Davenport, D. Takhar, J. N. Laska, T. Sun, K. F. Kelly, and R. G. Baraniuk, "Single-pixel imaging
41 via compressive sampling," *IEEE Signal Processing Magazine* **25**, 83-91 (2008).

- 1 7. W. L. Chan, K. Charan, D. Takhar, K. F. Kelly, R. G. Baraniuk, and D. M. Mittleman, "A single-pixel terahertz imaging
2 system based on compressed sensing," *Applied Physics Letters* **93**, 121105 (2008).
- 3 8. L. Gan, T. T. Do, and T. D. Tran, "Fast compressive imaging using scrambled block Hadamard ensemble," in *2008*
4 *16th European Signal Processing Conference (IEEE2008)*, pp. 1-5.
- 5 9. Z. Zhang, X. Wang, G. Zheng, and J. Zhong, "Hadamard single-pixel imaging versus Fourier single-pixel imaging,"
6 *Optics Express* **25**, 19619-19639 (2017).
- 7 10. S. S. Welsh, M. P. Edgar, R. Bowman, P. Jonathan, B. Sun, and M. J. Padgett, "Fast full-color computational imaging
8 with single-pixel detectors," *Optics Express* **21**, 23068-23074 (2013).
- 9 11. L. H. Bian, J. L. Suo, G. H. Situ, Z. W. Li, J. T. Fan, F. Chen, and Q. H. Dai, "Multispectral imaging using a single
10 bucket detector," *Scientific Reports* **6**, 24752 (2016).
- 11 12. F. Rousset, N. Ducros, F. Peyrin, G. Valentini, C. D'Andrea, and A. Farina, "Time-resolved multispectral imaging
12 based on an adaptive single-pixel camera," *Optics Express* **26**, 10550-10558 (2018).
- 13 13. P. Clemente, V. Duran, E. Tajahuerce, P. Andres, V. Climent, and J. Lancis, "Compressive holography with a single-
14 pixel detector," *Optics Letters* **38**, 2524-2527 (2013).
- 15 14. L. Martínez-León, P. Clemente, Y. Mori, V. Climent, J. Lancis, and E. Tajahuerce, "Single-pixel digital holography
16 with phase-encoded illumination," *Optics Express* **25**, 4975-4984 (2017).
- 17 15. K. Ota, and Y. Hayasaki, "Complex-amplitude single-pixel imaging," *Optics Letters* **43**, 3682-3685 (2018).
- 18 16. R. F. Liu, S. P. Zhao, P. Zhang, H. Gao, and F. L. Li, "Complex wavefront reconstruction with single-pixel detector,"
19 *Applied Physics Letters* **114**, 161901 (2019).
- 20 17. Y. Liu, J. Suo, Y. Zhang, and Q. Dai, "Single-pixel phase and fluorescence microscope," *Optics Express* **26**, 32451-
21 32462 (2018).
- 22 18. S. Shin, K. Lee, Y. Baek, and Y. Park, "Reference-Free Single-Point Holographic Imaging and Realization of an
23 Optical Bidirectional Transducer," *Physical Review Applied* **9**, 044042 (2018).
- 24 19. H. González, L. Martínez-León, F. Soldevila, M. Araiza-Esquivel, E. Tajahuerce, and J. Lancis, "High-speed single-
25 pixel digital holography," in *International Society for Optics and Photonics*(2017), p. 103330G.
- 26 20. H. Gonzalez, L. Martinez-Leon, F. Soldevila, M. Araiza-Esquivel, J. Lancis, and E. Tajahuerce, "High sampling rate
27 single-pixel digital holography system employing a DMD and phase-encoded patterns," *Optics Express* **26**, 20342-20350
28 (2018).
- 29 21. Z. Zhang, X. Ma, and J. Zhong, "Single-pixel imaging by means of Fourier spectrum acquisition," *Nature*
30 *Communications* **6**, 6225 (2015).
- 31 22. X. Y. Hu, H. Zhang, Q. Zhao, P. P. Yu, Y. M. Li, and L. Gong, "Single-pixel phase imaging by Fourier spectrum
32 sampling," *Applied Physics Letters* **114**, 051102 (2019).
- 33 23. S. Zhao, R. Liu, P. Zhang, H. Gao, and F. Li, "Fourier single-pixel reconstruction of a complex amplitude optical
34 field," *Optics Letters* **44**, 3278-3281 (2019).
- 35 24. G. A. Howland, D. J. Lum, M. R. Ware, and J. C. Howell, "Photon counting compressive depth mapping," *Optics*
36 *Express* **21**, 23822-23837 (2013).
- 37 25. M. Mir, B. Bhaduri, R. Wang, R. Y. Zhu, and G. Popescu, "Quantitative Phase Imaging," *Progress in Optics* **57**, 133-
38 217 (2012).
- 39 26. R. Shang, S. Chen, C. Li, and Y. Zhu, "Spectral modulation interferometry for quantitative phase imaging,"
40 *Biomedical Optics Express* **6**, 473-479 (2015).
- 41 27. A. S. Singh, A. Anand, R. A. Leitgeb, and B. Javidi, "Lateral shearing digital holographic imaging of small biological
42 specimens," *Optics Express* **20**, 23617-23622 (2012).
- 43 28. G. Popescu, *Quantitative phase imaging of cells and tissues* (McGraw Hill Professional, 2011).
- 44 29. K. Lee, K. Kim, J. Jung, J. Heo, S. Cho, S. Lee, G. Chang, Y. Jo, H. Park, and Y. Park, "Quantitative phase imaging

- 1 techniques for the study of cell pathophysiology: from principles to applications," *Sensors (Basel)* **13**, 4170-4191 (2013).
- 2 30. A. Kaczorowski, G. S. Gordon, and T. D. Wilkinson, "Adaptive, spatially-varying aberration correction for real-time
3 holographic projectors," *Optics Express* **24**, 15742-15756 (2016).
- 4 31. C. Liu, X. Yu, and M. K. Kim, "Phase aberration correction by correlation in digital holographic adaptive optics,"
5 *Applied Optics* **52**, 2940-2949 (2013).
- 6 32. R. Tatam, J. Davies, C. Buckberry, and J. Jones, "Holographic surface contouring using wavelength modulation of
7 laser diodes," *Optics Laser Technology* **22**, 317-321 (1990).
- 8 33. I. Yamaguchi, J. Kato, and H. Matsuzaki, "Measurement of surface shape and deformation by phase-shifting image
9 digital holography," in *19th Congress of the International Commission for Optics: Optics for the Quality of*
10 *Life*(International Society for Optics and Photonics2003), pp. 564-565.
- 11 34. Y. Saita, H. Shinto, and T. Nomura, "Holographic Shack–Hartmann wavefront sensor based on the correlation peak
12 displacement detection method for wavefront sensing with large dynamic range," *Optica* **2**, 411-415 (2015).
- 13 35. U. Schnars, C. Falldorf, J. Watson, and W. Jüptner, *Digital holography and wavefront sensing* (Springer, 2016).
- 14 36. A. Uesaka, K. Hayashi, T. Matsushita, and S. Arai, "3D atomic imaging by internal-detector electron holography,"
15 *Physical Review Letters* **107**, 045502 (2011).
- 16 37. G. Nehmetallah, and P. P. Banerjee, "Applications of digital and analog holography in three-dimensional imaging,"
17 *Advances in Optics and Photonics* **4**, 472-553 (2012).
- 18 38. S. Zhang, *Handbook of 3D machine vision: Optical metrology and imaging* (CRC press, 2013).
- 19 39. K. K. Tsia, K. Goda, D. Capewell, and B. Jalali, "Performance of serial time-encoded amplified microscope," *Optics*
20 *Express* **18**, 10016-10028 (2010).
- 21 40. Y. H. Feng, X. Lu, L. Song, X. Guo, Y. Wang, L. Zhu, Q. Sui, J. Li, K. Shi, and Z. Li, "Optical digital coherent
22 detection technology enabled flexible and ultra-fast quantitative phase imaging," *Optics Express* **24**, 17159-17167 (2016).
- 23 41. L. Song, Y. Feng, X. Guo, Y. Shen, D. Wu, Z. Wu, C. Zhou, L. Zhu, S. Gao, W. Liu, X. Zhang, and Z. Li, "Ultrafast
24 polarization bio-imaging based on coherent detection and time-stretch techniques," *Biomedical Optics Express* **9**, 6556-
25 6568 (2018).
- 26 42. K. Creath, "Phase-shifting holographic interferometry," in *Holographic Interferometry*(Springer, 1994), pp. 109-150.
- 27 43. U. Schnars, "Direct phase determination in hologram interferometry with use of digitally recorded holograms,"
28 *Journal of the Optical Society of America* **11**, 2011-2015 (1994).
- 29 44. Y. Kikuchi, D. Barada, T. Kiire, and T. Yatagai, "Doppler phase-shifting digital holography and its application to
30 surface shape measurement," *Optics Letters* **35**, 1548-1550 (2010).
- 31 45. M. J. Sun, L. T. Meng, M. P. Edgar, M. J. Padgett, and N. Radwell, "A Russian Dolls ordering of the Hadamard basis
32 for compressive single-pixel imaging," *Scientific Reports* **7**, 3464 (2017).
- 33 46. W. H. Lee, "Binary synthetic holograms," *Applied Optics* **13**, 1677-1682 (1974).
- 34 47. S. A. Goorden, J. Bertolotti, and A. P. Mosk, "Superpixel-based spatial amplitude and phase modulation using a digital
35 micromirror device," *Optics Express* **22**, 17999-18009 (2014).
- 36 48. L. Tian, Z. J. Liu, L. H. Yeh, M. Chen, J. S. Zhong, and L. Waller, "Computational illumination for high-speed in vitro
37 Fourier ptychographic microscopy," *Optica* **2**, 904-911 (2015).
- 38 49. S. Liu, J. A. Mulligan, and S. G. Adie, "Volumetric optical coherence microscopy with a high space-bandwidth-time
39 product enabled by hybrid adaptive optics," *Biomedical Optics Express* **9**, 3137-3152 (2018).
- 40 50. P. G. Vaz, D. Amaral, L. F. Requiça Ferreira, M. Morgado, and J. Cardoso, "Image quality of compressive single-
41 pixel imaging using different Hadamard orderings," *Optics Express* **28**, 11666-11681 (2020).
- 42

Figures

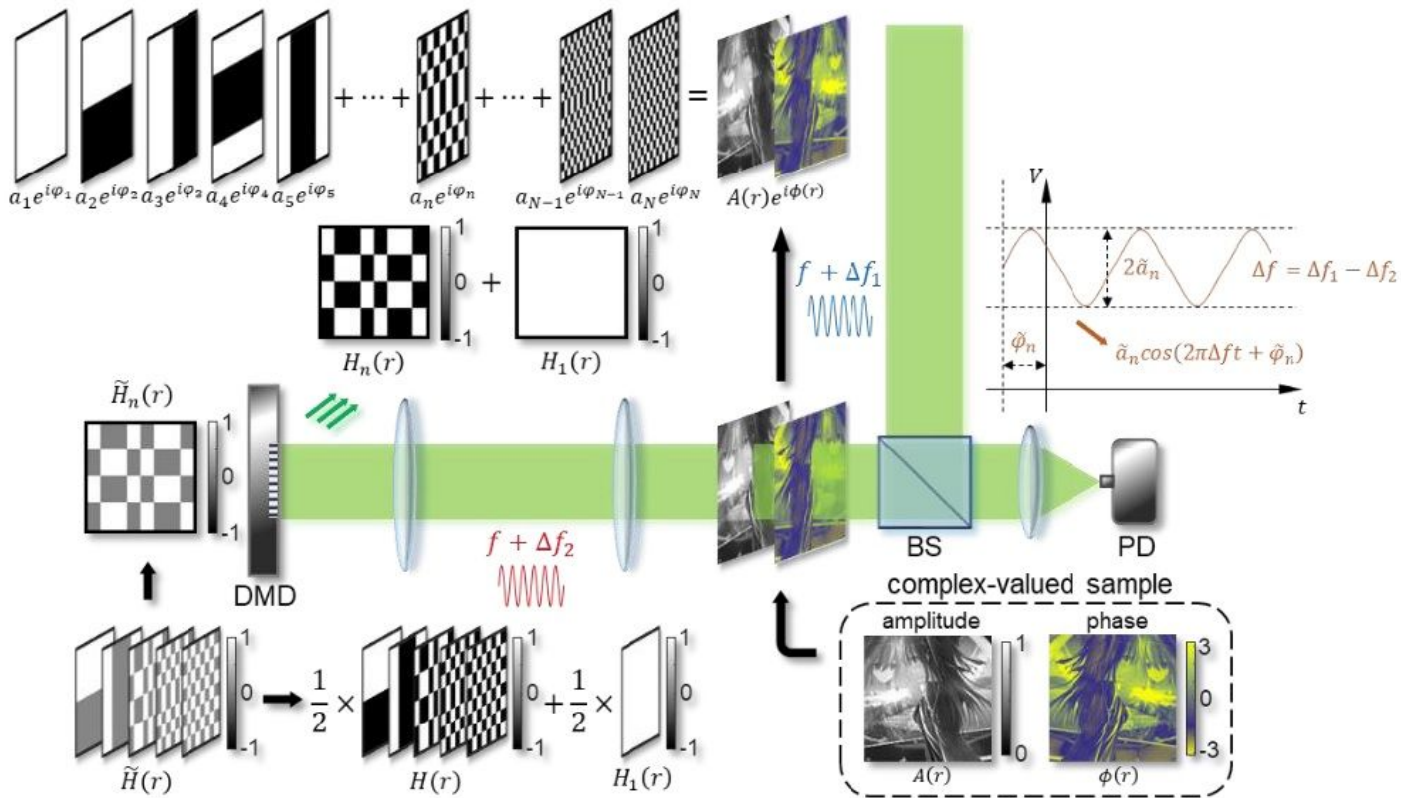


Figure 1

Principle diagram of the high-throughput single-pixel compressive holography. A complex-valued object $\tilde{H}(r) = A(r)e^{i\phi(r)}$ can be expressed as the superposition of a complete set of orthogonal Hadamard basis $H_n(r)$ with corresponding coefficients. To retrieve these coefficients, one can illuminate the 31 object with a series of Hadamard-like patterns $H_n(r)$ (with components "0" and "1") generated by the DMD. To implement heterodyne holography, a beat frequency Δf is introduced between the signal beam and the reference beam, enabling a time-varying signal that can be measured by the photodiode. The simple 1 linear transformation between $\tilde{H}_n(r)$ and $H_n(r)$ allows the reconstruction of holographic images with pure amplitude patterns. DMD: digital micromirror device; 2 BS: beam splitter; PD: photodiode.

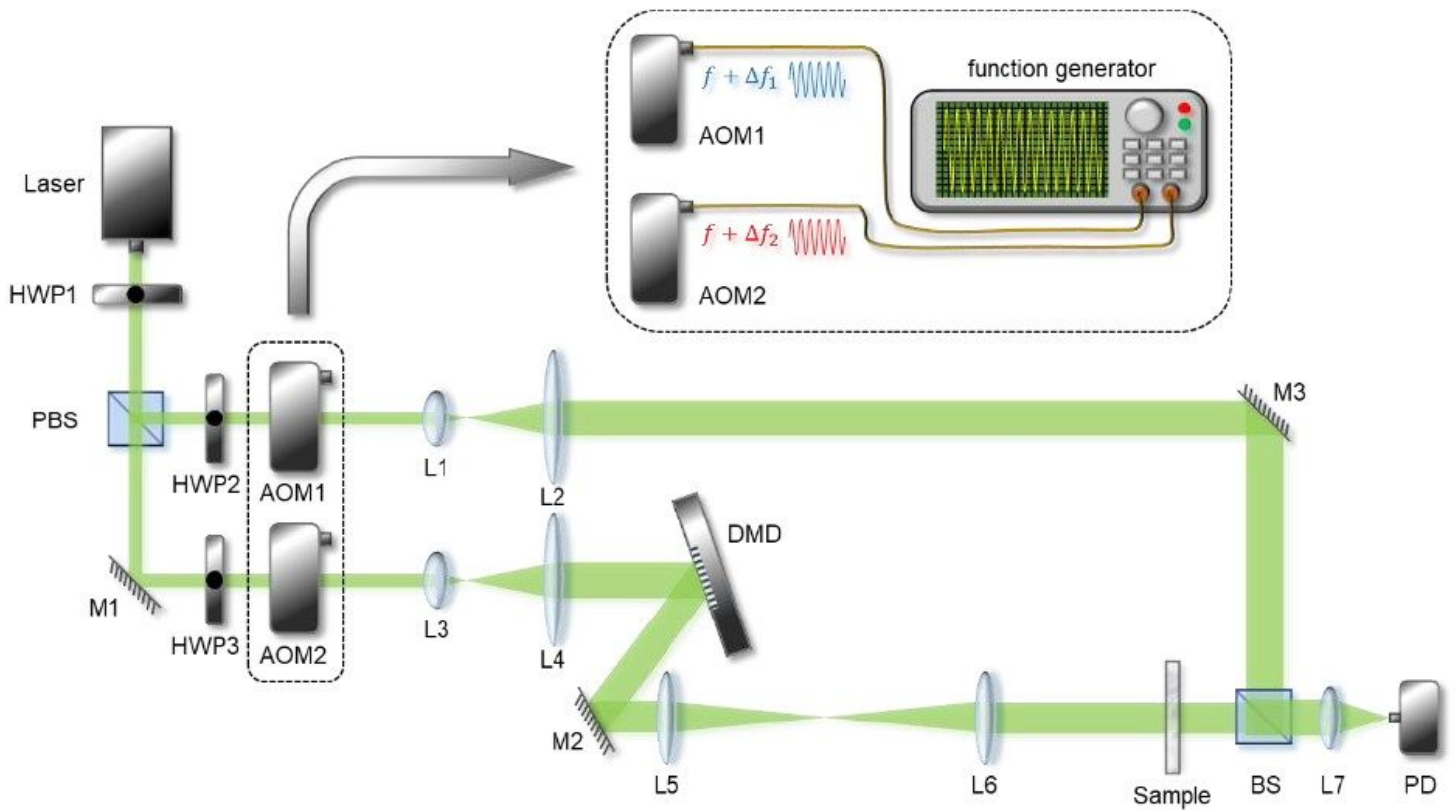


Figure 2

Experiment setup of the high-throughput single-pixel compressive holography system. A series of Hadamard-like patterns were generated and projected to the sample. HWP1-3: half-wave plate; M1-3: mirror; PBS: polarization beam splitter; AOM1-2: acousto-optic modulators that cause a frequency shift to the light passing through; L1-7, lenses ($\varnothing_1 = \varnothing_3 = 7.5$ mm, $\varnothing_2 = \varnothing_4 = 250$ mm, $\varnothing_7 = 150$ mm, \varnothing_5 and \varnothing_6 is scalable to be adapted for various demands); DMD: digital micromirror device that provides amplitude modulation with “0” and “1”; BS: beam splitter; PD: photodiode. The upper inset shows the detailed procedure of how a double-channel function generation generates a beating frequency to drive the AOMs (an electronic power amplifier is omitted here).

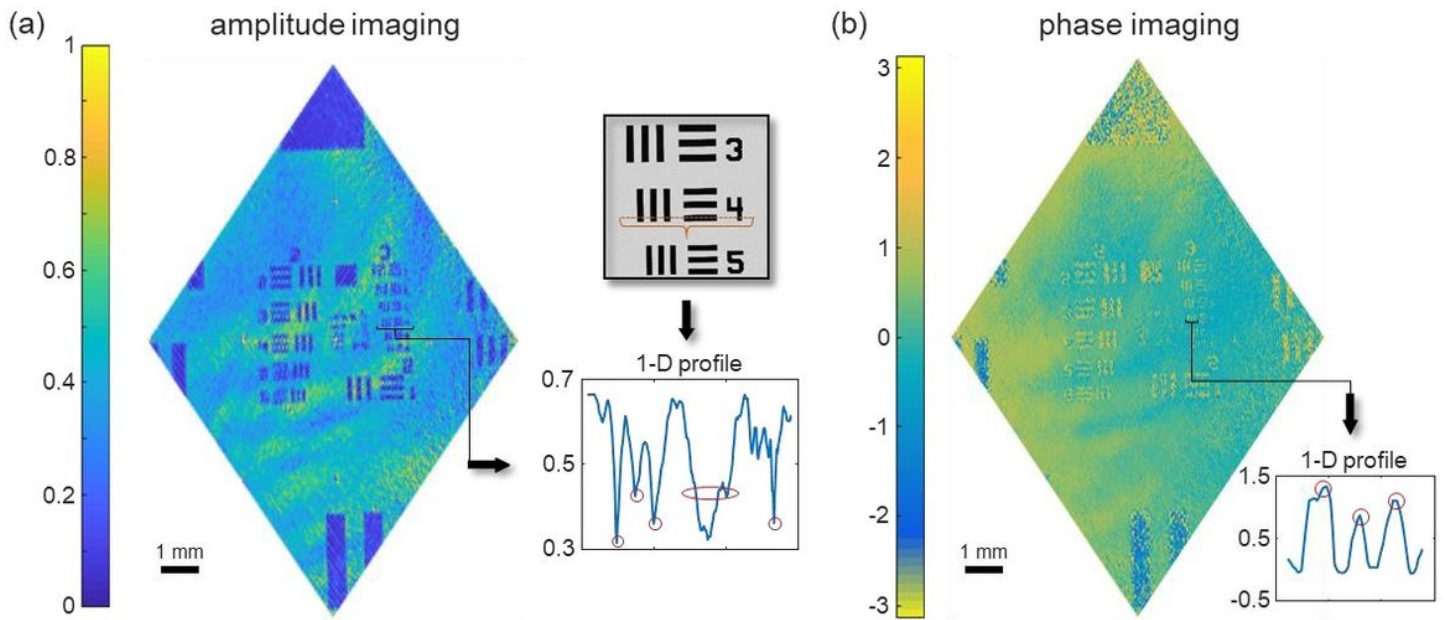


Figure 3

Performance of the high-throughput SPH in large FOV mode. A standard positive 1951-USAF resolution test target (Thorlabs R3L3S1P) is used as a testing sample. 3×3 pixels binning strategy was adopted for 768×768 pixels, leading to 256×256 superpixels. (a) Reconstructed amplitude image of the resolution target. The upper inset: the image captured by conventional microscopy; the lower inset: the corresponding one-dimensional (1D) profile of element 4 of group 3. (b) Reconstructed phase image of the resolution test target. The corresponding 1D profile is shown in the inset

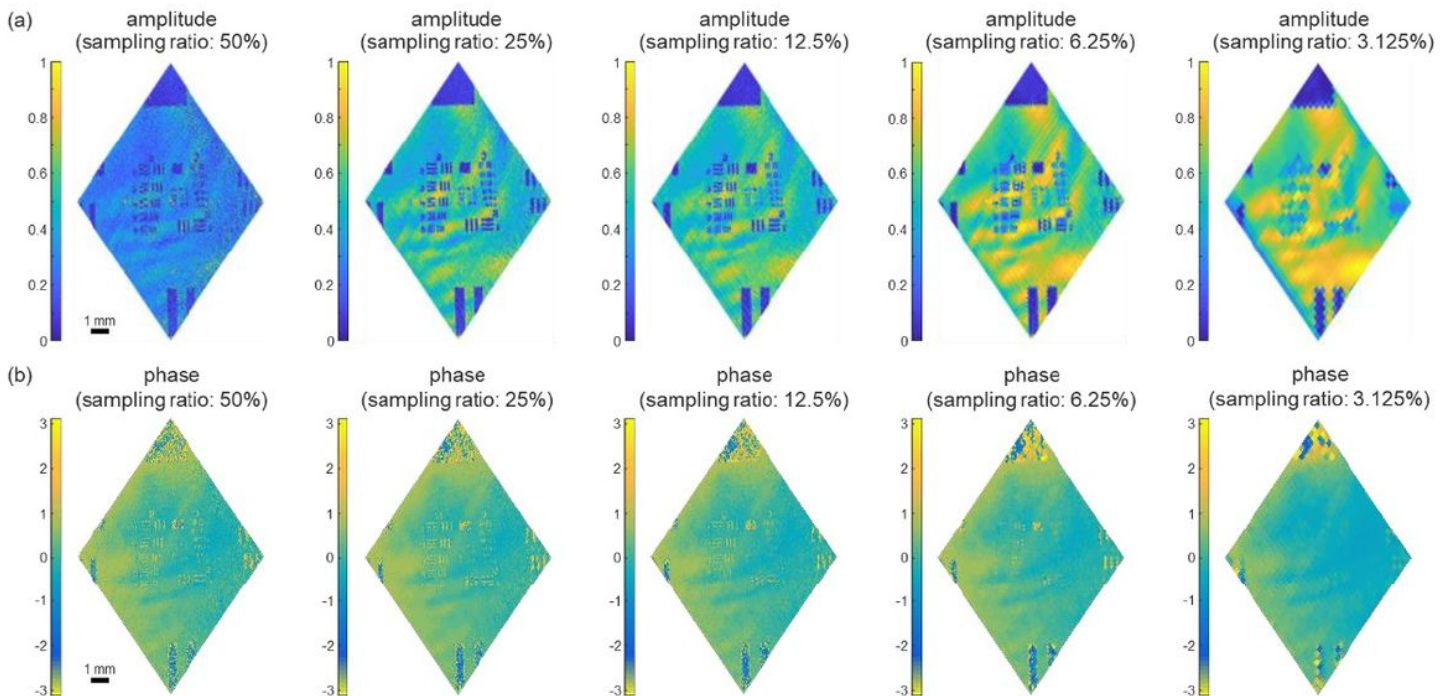


Figure 4

Reconstruction of holographic images for the resolution target with compressive sensing. The amplitude and wrapped phase images are reconstructed with different sampling ratios of 50%, 25%, 12.5%, 6.25%, 3.125%.

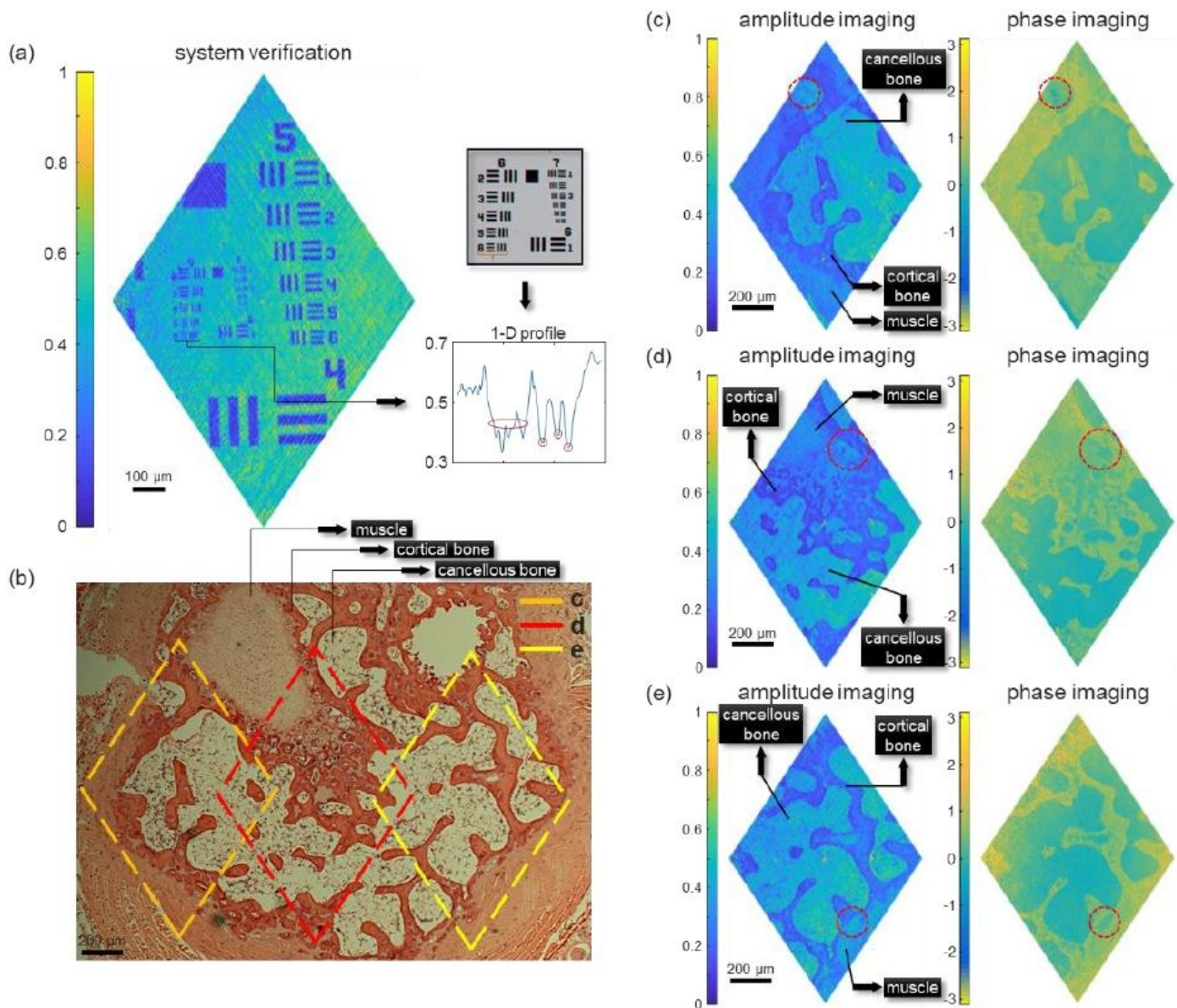


Figure 5

Performance of the high-throughput SPH in high-resolution mode. (a) Reconstructed amplitude image of a resolution target. The upper inset: the image of the resolution target (containing groups 6 and 7) captured by a conventional microscope; the lower inset: the corresponding one-dimensional (1D) profile of element 6 of group 6. (b) The image of a slice of stained tissue from rat tail, captured using a conventional microscope. Three diamond-shaped boxes represent the area being measured by the holographic system. (c)-(e) The reconstructed amplitude and phase images for different parts of the stained tissue.

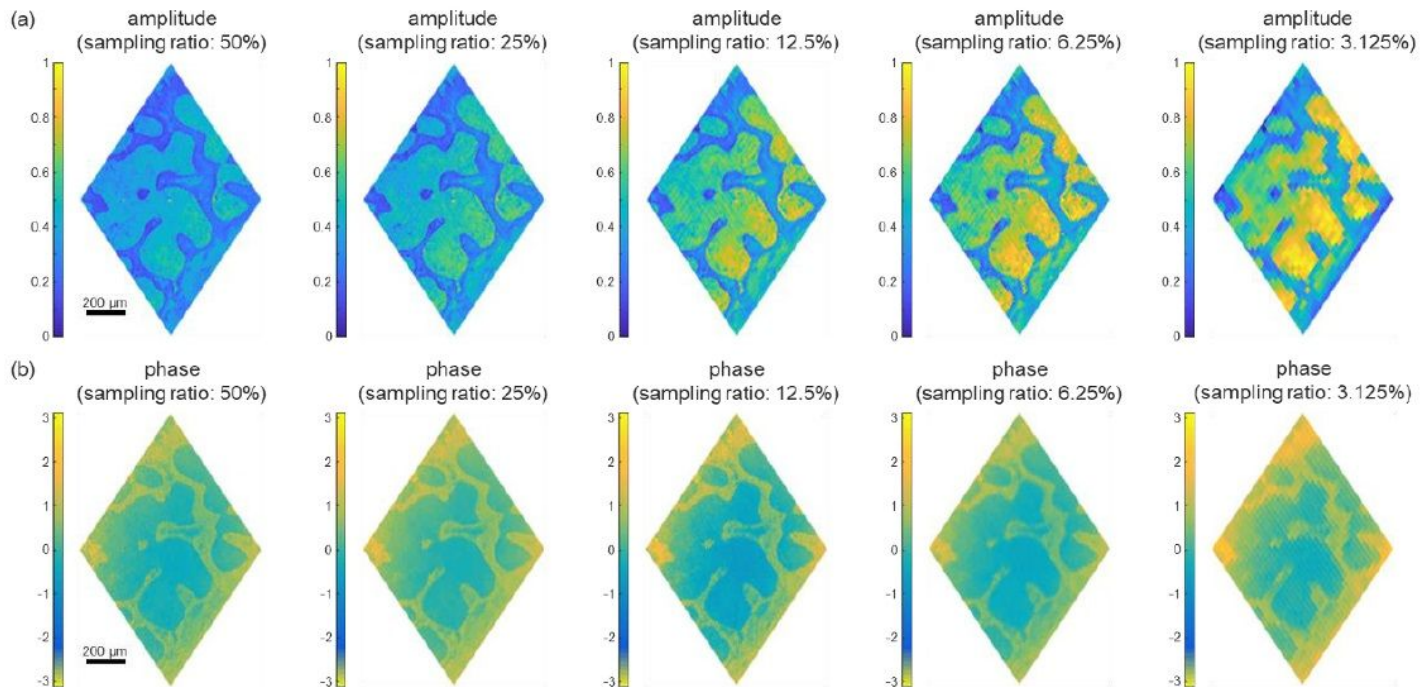


Figure 6

Reconstruction of holographic images for the piece of rat tail with compressive sensing. The amplitude and wrapped phase images are reconstructed with different sampling ratios of 50%, 25%, 12.5%, 6.25%, 3.125%.

Supplementary Files

This is a list of supplementary files associated with this preprint. Click to download.

- [dataandsupportingfiles.zip](#)